Environmental and Climate Technologies
2025, vol. 29, no. 1, pp. 865–879
https://doi.org/10.2478/rtuect-2025-0058
https://content.sciendo.com

1862
RIGA TECHNICAL
UNIVERSITY

Mechanisms and Characteristics of Thermodynamically Quasistable Structure Formation in Metals

Anatoliy PAVLENKO[1]*, Borys BASOK[2]

[1]*Kielce University of Technology, aleja Tysiąclecia Państwa Polskiego, 7, 25-314, Kielce, Poland*
[1,2]*Institute of Engineering Thermophysics, National Academy of Sciences, Kiew, Ukraine*

Received 09.09.2025; accepted 21.10.2025

***Abstract* – This paper investigates the processes of thermodynamic pseudostability (metastability) in liquid metals during rapid solidification, a mechanism that results in the formation of an amorphous structure. Established technologies for creating bulk amorphous materials are typically limited to producing only a thin amorphous layer. This limitation stems from the thermal inertia of the materials, which inherently tend towards thermodynamic equilibrium. In the present study, a novel approach is proposed to intensify heat exchange by utilizing inoculants within the liquid melts combined with high-velocity cooling. To facilitate process prediction and optimization, a mathematical model of the massive amorphous layer formation process is introduced. This model allows for the accurate prediction of the amorphization process evolution and subsequent optimization of the critical technological parameters.**

***Keywords* – Amorphous structure; heat and mass transfer; thermal conductivity; thermodynamic stability.**

1. INTRODUCTION

The amorphous state of materials is characterized by their thermodynamic metastability and chaotic atomic packing. This isotropic local structure dictates unique physicochemical properties that often surpass those of crystalline materials in various technical applications. Amorphous structures in metals (ASM) represent a relatively new class of non-crystalline materials with significant promise for the production of micrometallic products [1]–[3]. This structure is traditionally achieved by incorporating alloying elements with differing atomic sizes under conditions of rapid cooling of the liquid phase to a solid state [4], [5]. During this process, the alloy solidifies in a non-crystalline (amorphous) state.

The required cooling rate inherently imposes limitations on the thickness of the amorphous layer, typically restricting the final product to thin ribbons, foils, and similar geometries [6], [7]. However, recent studies indicate that advanced technologies have allowed for the production of amorphous metals with thicknesses approaching 1 mm [8]–[10]. The authors of this work emphasize that bulk amorphization technologies are highly promising because the material can be formed at the micrometre scale while retaining superior properties.

---

* Corresponding author.
E-mail address: apavlenko@tu.kielce.pl

The solidification time is another critical parameter that profoundly influences the process of amorphous structure formation [11], [12].

Overall, the formation of ASM is not a straightforward process and, therefore, currently remains an active subject of ongoing research [13]–[20]. Amorphous structures in metals (ASM) exhibit high strength, superior corrosion resistance [21]–[24], high elastic limit, and various other beneficial properties compared to traditional crystalline alloys. However, outstanding challenges related to structural stability still persist [25], [26] and require resolution. For instance, it is known that ASM are susceptible to degradation influenced by technological parameters and mechanical post-processing [27], [28]. Previous studies [29]–[33] have demonstrated the influence of cooling rate on material structure and noted that modifying the cooling intensity can promote the formation of two distinct phases: a homogeneous (amorphous) phase and a heterogeneous (partially crystalline) phase.

Ultra-rapid cooling of liquids promotes the formation of a homogeneous phase, while subsequent isothermal aging of the undercooled liquid leads to the development of a metastable heterogeneous phase.

Similar challenges in obtaining Amorphous Structures in Metals (ASM) are inherent to nearly all established methods of amorphous structure formation, which can generally be classified as follows:

- rapid solidification from the melt [34]–[37];
- pulsed laser quenching [38]–[41];
- powder metallurgy techniques [42]–[46];
- magnetron sputtering [47]–[50].

Thus, ASM are typically produced via liquid quenching, where the fundamental mechanism for amorphous structure formation is the suppression of crystallization nucleation through rapid liquid cooling. This approach presents a major challenge: achieving the necessary cooling rate for bulk materials is inherently difficult. Consequently, researchers typically combine various techniques to attain the optimal heat exchange intensity.

To address this limitation and obtain massive amorphous structures, we developed a novel laboratory experimental setup. This system was used to investigate the production of bulk amorphous materials via the rapid cooling of molten alloys combined with the addition of pre-cooled inoculants. The essence of this technology lies in realizing internal heat removal (heat extraction) and generating additional active cooling centers within the melt on the inoculant surfaces. This process, driven by heat transfer and the melting of the inoculants, enhances the solidification rate and promotes predominantly volumetric solidification. This technology is distinct primarily due to its implementation of internal heat removal using localized heat sinks.

The development of an industrial technology for synthesizing ASM with inoculant addition would require significant expenditure of time and material resources. These costs can be substantially reduced by employing mathematical modeling methods. Such models will allow for a comprehensive analysis of the ASM formation processes and enable the quantitative determination of the inoculants' influence on the degree of melt amorphization.

2. THEORETICAL DESCRIPTION OF THE ASM FABRICATION TECHNOLOGY

To execute the theoretical analysis of the proposed technology, a mathematical model is introduced. This model is designed to describe the first-order phase transition processes occurring during the intensive cooling of the melt. To enhance this cooling intensity, pre-cooled metal particles are introduced into the melt, which serve as localized heat sink centers. This procedure is expected to yield a melt cooling rate sufficient for Amorphous Structure in Metals (ASM) formation in select alloys. The overall solidification process can be distinctly divided into three separate stages (Fig. 1), which will be examined in detail below.

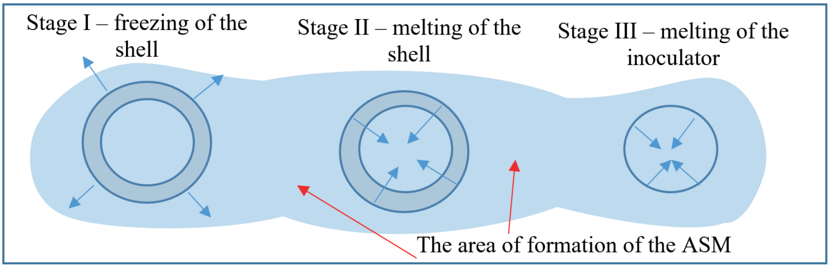

Fig. 1. Computational Scheme.

The solidification process can be analyzed across three distinct stages.

Stage I: shell formation and melting.

During the initial period (Stage I, Fig. 1), upon submersion of the inoculant into the melt, a solid metal shell forms instantaneously on its surface. The thermal energy transferred from the surrounding melt is consumed by two concurrent processes: heating the inoculant core and melting the newly formed solid shell. This stage concludes precisely at the moment the solid shell completely remelts.

Stage II: inoculant preheating.

In the second stage, the solid inoculant core continues to absorb heat from the surrounding liquid melt. During this period, the inoculant is heated up until it reaches its melting temperature while remaining in direct contact with the liquid phase.

Stage III: inoculant dissolution and volumetric cooling.

In the third stage, the inoculant begins to melt, and the resulting liquid phase dissolves into the main melt volume. The primary objective of implementing this technology is to achieve critical cooling rates for the melt, specifically in the order of 10^4 °C/s. At such high cooling velocities, the crystalline structure formation is suppressed, ensuring the material remains in a state of thermodynamic non-equilibrium upon achieving its solid state.

2.1. Formation and Melting of the Shell on the Inoculant Surface

This period of melting is described by a system of heat conduction equations for a two-layer body [51]–[54], which is applicable for the time interval $\tau > \tau_1 + \tau_2$. This system includes separate equations for the material of the inoculant core ($0 \le r < R_1$) and for the melt shell ($R_1 \le r < R_2$):

$$\begin{cases} c_i(T)\rho_i(T)\dfrac{\partial T_i(r,\tau)}{\partial \tau} = \dfrac{1}{r^2}\dfrac{\partial}{\partial r}\left[r^2\lambda_i(T)\dfrac{\partial T_i(r,\tau)}{\partial r}\right], 0 \le r < R_1 \\ c_m(T)\rho_m(T)\dfrac{\partial T_m(r,\tau)}{\partial \tau} = \dfrac{1}{r^2}\dfrac{\partial}{\partial r}\left[r^2\lambda_m(T)\dfrac{\partial T_m(r,\tau)}{\partial r}\right], R_1 \le r < Z_2 \end{cases}, \qquad (1)$$

where R_2 is defined as the radius of the inoculant core combined with the melt shell.

The boundary conditions applicable at $\tau = \tau_1 + \tau_2$ are as follows:

$$\frac{\partial T_i(0,\tau)}{\partial r} = 0; r = 0, \tag{2}$$

$$\lambda_i(T)\frac{\partial T_i(R_i,\tau)}{\partial r} = \lambda_m(T)\frac{\partial T_m(R_2,\tau)}{\partial r}, \quad T_i(R_1,\tau) = T_2(R_2,\tau), r = R_2. \tag{3}$$

Boundary condition for heat exchange at the melt shell–bulk melt interface ($r = R_2$):

$$-\rho_m(T)Q_m\frac{\mathrm{d}R_2(\tau)}{\mathrm{d}\tau} = \alpha_m\left(T(\tau) - T_{f0}\right) - \lambda_m(T)\frac{\partial T_m(R(\tau),\tau)}{\partial r}, \tag{4}$$

$$T_i(R_2(\tau),\tau) = T_l^i, \; 0 \le R_2(\tau) \le R_1, \tau > \tau_2, \; R_2(\tau) > R_i, \tau > \tau_1 + \tau_2.$$

Initial conditions:

$$\begin{cases} T_i(r,\tau_1+\tau_2) = \phi_i(r,\tau_1+\tau_2), 0 \le r < R_1 \\ R_2(\tau_1+\tau_2) = R_i \end{cases}, \tag{5}$$

where $\phi_i(r,\tau_1+\tau_2)$, is the solution to the heat conduction problem for the inoculant material under the condition $\tau = \tau_1 + \tau_2$.

The duration of Stage I concludes when the melt shell that formed on the inoculant surface is completely remelted.

Calculation algorithm. The temperature values at the internal points of the computational domain ($1 \le k \le N-1$) are determined using Eq. (6) and Eq. (7), derived from the finite difference analog of the system of equations (1):

$$\frac{T_i^{k+1} - T_i^k}{\Delta\tau} = \frac{2}{\Delta r^2 \rho_i^k c_i^k}\left[\frac{T_{i-1}^k - T_i^k}{\frac{1}{\lambda_{i-1}^k} + \frac{1}{\lambda_i^k}} - \frac{T_i^k - T_{i+1}^k}{\frac{1}{\lambda_i^k} + \frac{1}{\lambda_{i+1}^k}} + \frac{2}{i}\frac{T_{i+1}^k - T_{i-1}^k}{\frac{1}{\lambda_{i+1}^k} + \frac{1}{\lambda_{i-1}^k}}\right], \tag{6}$$

where the thermophysical parameters (λ_i^k, ρ_i^k, c_i^k) are determined from the previous time layer, denoted by the index k.

The Boundary Condition (2), when represented in the finite difference approximation with second-order accuracy, is presented in the form:

$$\frac{T_0^{k+1} - T_0^k}{\Delta\tau} = \frac{2\left(T_1^k - T_0^k\right)}{\Delta r^2 \rho_0^k c_0^k}\frac{\lambda_0^k \lambda_1^k}{\lambda_0^k + \lambda_1^k}. \tag{7}$$

The movement of the external boundary associated with the formation and subsequent melting of the metal melt shell is accounted for by calculating Eq. (8). The computation using the prescribed algorithm is deemed complete when, during the shell melting process, the value of the grid node count N becomes equal to N_0.

$$T^{k+j} = T_{f0} + \frac{\Delta\tau}{\rho_i^k c_i^k \Delta r}\left[\alpha\left(T_p^k - T_{f0}\right) + \frac{\lambda_i^k}{\Delta r}\left(T_{i-1}^k - T_{f0}\right)\right], \tag{8}$$

where T_{f0} is the zero-fluidity temperature of the metal, α is the heat transfer coefficient from the melt to the inoculant surface.

Next, the value of the time step (Δτ) is determined $\overline{S} = T_{f0} - T^{k+j}$. The formation of the metal melt begins when $\overline{S} > 0$. This state is reached after k_1 time steps, provided the following condition is satisfied:

$$\sum_{j=1}^{k_1}\left(T_{f0} - T^{k+j}\right) \geq Q/c_i^{k+1}. \tag{9}$$

Upon satisfying this condition, a layer of thickness Δ*r* is formed.

The shell melting process occurs when $\overline{S} < 0$. After the completion of k_2 time steps, and upon satisfying the condition:

$$\sum_{j=1}^{k_2}\left(T^{k+j} - T_{f0}\right) \geq \frac{Q}{c_N^{k+1}}, \tag{10}$$

a layer of thickness Δ*r* is melted. Consequently, the number of layers in the computational scheme (*N*) is decremented by one.

2.2. Inoculant Melting

The melting process of the inoculant material commences once its surface has been preheated to the melting temperature.

The preheating of the inoculant body is governed by the heat conduction equation for the inoculant material under the condition $\tau > \tau_1 + \tau_2 + \tau_3$:

$$c_i(T)\rho_i(T)\frac{\partial T_i(r,\tau)}{\partial\tau} = \frac{1}{r^2}\frac{\partial}{\partial r}\left[r^2\lambda_i(T)\frac{\partial T_i(r,\tau)}{\partial\tau}\right], 0 \leq r < R_2. \tag{11}$$

Boundary conditions at $\tau > \tau_1 + \tau_2 + \tau_3$:

$$(r = 0),\ \frac{\partial T_i(0,\tau)}{\partial r} = 0. \tag{12}$$

Heat transfer condition at the inoculant surface–melt interface ($r = R_2$):

$$\lambda_i(T)\frac{\partial T_i(R_2,\tau)}{\partial r} = \alpha_m\left[T\upsilon - T_i(R_2,\tau)\right]. \tag{13}$$

Initial conditions:

$$\begin{cases} T_i(r,\tau_1+\tau_2+\tau_3) = \phi_i(r,\tau_1+\tau_2+\tau_3), 0 \leq r < R_2 \\ R_2(\tau_1+\tau_2+\tau_3) = R_i \end{cases}, \tag{14}$$

where $\phi_i\left(r,\tau_1+\tau_2+\tau_3\right)$ is the solution to the heat conduction problem for the inoculant material, as described in Stage III, under the condition $\tau=\tau_1+\tau_2+\tau_3$. The total duration of the period required to preheat the body's surface to the melting temperature is denoted by τ_4. Following the preheating of the inoculant surface, the melting process commences. This phase is governed by the heat conduction equation for the casting material (Eq. 11) at $\tau>\tau_1+\tau_2+\tau_3+t_4$.

Heat transfer condition at the inoculant surface–melt interface ($r = R_i$):

$$-\rho_i(T)Q_i\frac{\mathrm{d}R_i(\tau)}{\mathrm{d}\tau}=\alpha_m\left(T(\tau)-T_L\right)-\lambda_i(T)\frac{\partial T_i\left(R_i(\tau),\tau\right)}{\partial r},$$

$$T_i\left(R_i(\tau),\tau\right)=T_L,\ 0\le r<R_i,\ \tau>\tau_1+\tau_2+\tau_3+\tau_4. \tag{15}$$

Initial conditions:

$$T_i\left(r,\tau_1+\tau_2+\tau_3+\tau_4\right)=\phi_i\left(r,\tau_1+\tau_2+\tau_3+\tau_4\right),\ 0\le r<R_i, \tag{16}$$

where $\phi_i\left(r,\tau_1+\tau_2+\tau_3+\tau_4\right)$ is the solution to the heat conduction problem for the inoculant material, as described during the period of preheating the inoculant surface to the melting temperature, under the condition $\tau=\tau_1+\tau_2+\tau_3+\tau_4$.

2.3. Calculation Algorithm

The temperature values at the internal points of the computational domain ($0 \le k \le N_0^{-1}$) are determined using (6) and (7). The temperature at the boundary point N_0 is calculated from the finite difference analog of the boundary condition (13):

$$\rho_{N_0}^k c_{N_0}^k\frac{T_{N_0}^{k+1}-T_{N_0}^k}{\Delta\tau}=\alpha\left(T^k-T_{N_0}^k\right)-\frac{T_{N_0}^k-T_{N_0-1}^k}{\dfrac{\Delta r}{2\lambda_{N_0}^k}+\dfrac{\Delta r}{2\lambda_{N_0-1}^k}}. \tag{17}$$

The calculation for the melting of the body's solid phase commences when the temperature value $T_{N_0}^{k+1}$ becomes equal to the inoculant's melting temperature, T_l.

The temperature values at points $0 < k < N$ are determined using Eq. (6) and Eq. (7). The movement of the external melting boundary is accounted for using the following equation:

$$T^{k+j}=T_l+\frac{\Delta\tau}{\rho_N^k c_N^k\Delta r}\left[\alpha\left(T^k-T_l\right)+\frac{\lambda_N^k}{\Delta r}\left(T_{N-1}^k-T_l\right)\right]. \tag{18}$$

A layer of thickness Δr is considered to be completely melted when, after the completion of k_3 time steps and upon satisfying the condition $\overline{S}<0$, the following equation is fulfilled:

$$\sum_{j=1}^{k_3}\left(T^{k+j}-T_l\right)\geq \frac{Q}{c_N^{k+j}}. \tag{19}$$

The calculation for the complete melting of the body is concluded when the number of layers in the computational scheme reaches $N = 1$.

The results of this calculation are presented in Figs. 2–4.

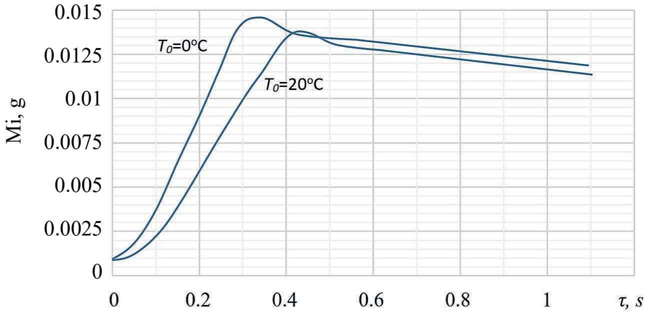

Fig. 2. The time-dependent mass of the $Cu_{45}Ti_{35}Zr_{20}$ inoculant with an initial radius $R_0 = 0.5$ mm at two distinct initial inoculant temperatures (T_0): 0 °C and 20 °C.

For this study, model materials were selected based on their known propensity for amorphization. This tendency is due to the inclusion of easily amorphizing elements, such as Zr, B, P, and Si. Additionally, certain alloys from the Fe and Co groups were chosen, incorporating metalloid glass-forming additives like B, P, Si, and C. The thermophysical properties of the investigated alloys are summarized in Table 1.

TABLE 1. THERMOPHYSICAL PROPERTIES OF THE INVESTIGATED ALLOYS

Alloy	**Melting temperature, °C**	**Glass transition temperature, К**	**Alloy density, кg/m^3**	**Alloy specific heat capacity, J/(kg·K)**	**Thermal conductivity coefficient, W/(m·K)**
$Fe_{80}P_{13}C_7$	985	463	6690	720	38.5
$Co_{75}Si_{15}B_{10}$	1120	512	7290	850	40
$Ni_{62,4}Nb_{37,6}$	1169	672	7850	609	69
$Cu_{45}Ti_{35}Zr_{20}$	1090	410	6900	513.9	175

The results of the calculations demonstrate incomplete melting of the $Cu_{45}Ti_{35}Zr_{20}$ inoculants. While a sufficient cooling intensity near the heat exchange boundaries and between the inoculants may yield a thin ASM layer, achieving bulk (volumetric) ASM using this particular alloy system remains unattainable. An analogous result was obtained for the $Ni_{62,4}Nb_{37,6}$ alloy (Fig. 3).

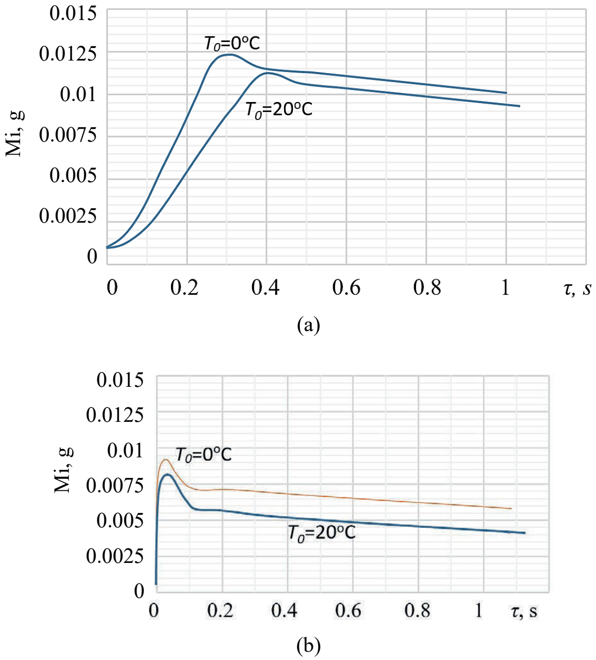

Fig. 3. Time-dependent mass of the inoculants with an initial radius $R_0 = 0.5$ mm at two distinct initial inoculant temperatures (T_0) 0°C and 20 °C: a) $Ni_{62,4}Nb_{37,6}$; b) $Fe_{80}P_{13}C_7$.

In contrast to the previous findings, the implementation of the technology using inoculants made of the $Co_{75}Si_{15}B_{10}$ (Fig. 4) successfully demonstrates complete inoculant melting. This complete dissolution is a crucial indicator, suggesting that the technique, when applied with this specific alloy system, is capable of achieving bulk ASM formation.

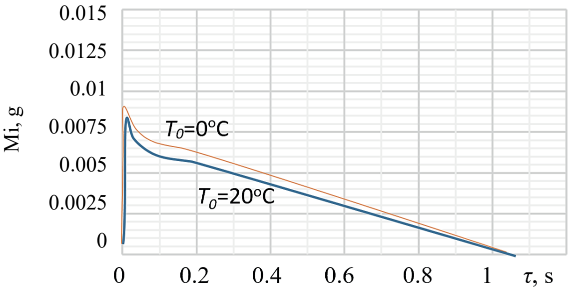

Fig. 4. Time-dependent mass of the $Co_{75}Si_{15}B_{10}$ inoculant with an initial radius R_0 = 0.5 mm at two distinct initial inoculant temperatures (T_0): 0 °C and 20 °C.

In summary, the technology involving the high-velocity solidification of a melt within a cooled mold, coupled with the introduction of inoculants, operates by achieving two key objectives: promoting internal heat extraction and forming additional active cooling centers throughout the melt volume.

The influence of the inoculants is evidenced by an increased overall solidification rate and the development of predominantly volumetric solidification. Consequently, the metallic melt containing the introduced inoculants is characterized by an undercooled state across the entire material volume. The inoculants not only remove initial superheat but also actively contribute to the sustained undercooling of the melt.

4. EXPERIMENTAL VERIFICATION OF THE MODEL

To investigate the governing factors and mechanisms for the formation of bulk ASM, a dedicated experimental setup (Fig. 5) was developed. This apparatus facilitates the high-velocity cooling and solidification of the metallic melt.

The main mold is encircled by a heat exchanger (pos. 2), which provides the rapid cooling required for the melt. Simultaneously with the introduction of the melt (pos. 6), inoculants (pos. 8) are injected into the system. During the solidification process, the metal is subjected to ultrasonic treatment (pos. 7). This ultrasonic agitation serves to further suppress the nucleation and growth of any crystalline structure, thereby enhancing the amorphization tendency.

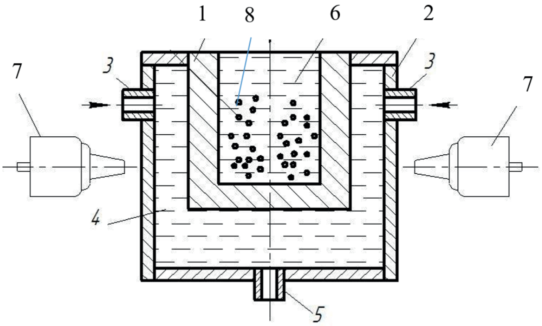

Fig. 5. Schematic diagram of the experimental research setup. The components are designated as follows: 1 – coled mold, 2 – heat exchanger, 3 – cooling fluid supply, 4 – water; 5 – water outlet, 6 – melt, 7 – ultrasonic emitter, 8 – inoculants.

The high-intensity mechanical oscillations generated by the ultrasonic emitter (pos. 7) induce bulk waves. These waves traverse the walls of the confining structure (pos. 2) and the copper cooling mold (pos. 1), consequently affecting the melt.

Crucially, at the moment of contact between a solid inoculant particle and the liquid metal, localized thermal undercooling is instantaneously created within the melt. This occurs even when the overall melt volume exhibits significant superheat.

The experimental investigations were conducted under the conditions previously established in the computational models (as presented in Figs. 2–4). The alloys studied were $Cu_{45}Ti_{35}Zr_{20}$, $Ni_{62,4}Nb_{37,6}$, $Fe_{80}P_{13}C_{7}$, $Co_{75}Si_{15}B_{10}$, all of which were prepared from powder components. Only high-purity master alloy materials were used for the preparation of these final alloys.

To analyse the material structure and quantify the degree of amorphization, several samples were extracted. These templates were strategically positioned to allow for the determination of structural variation across a series of transverse cross-sections.

Microstructural analysis was performed following chemical etching, utilizing an etchant composed of CH_3-COOH, HNO_3, and HF. The degree of amorphization was subsequently determined using electron-microscopic investigations in the direct expansion mode. An

MMP−4 microscope was employed for the visual inspection and photomacrography of the prepared cross-sections.

The metallographic investigations revealed that the studied metal layers, obtained by melt cooling under the conditions corresponding to Fig. 2 and Fig. 3, predominantly exhibit a microcrystalline, ferritic structure (Fig. 6). The formation of the ASM was observed exclusively at the cooled boundaries. A similar outcome was achieved for the $Co_{75}Si_{15}B_{10}$, though the amorphous layers were significantly wider (Fig. 6(c)).

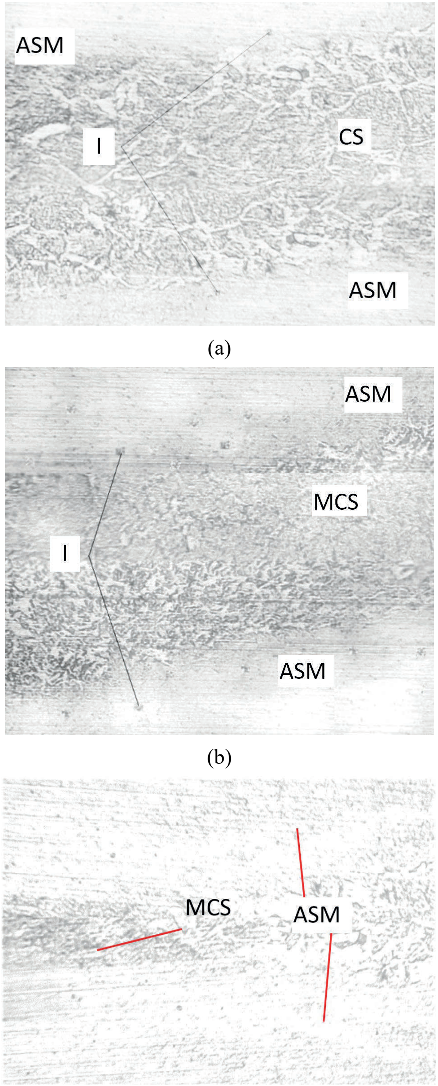

(a)

(b)

(c)

Fig. 6. Microstructure of the solidified metal containing 20 % volume fraction of inoculants. The images illustrate the structural differences based on alloy composition: a) $Cu_{45}Ti_{35}Zr_{20}$; b) $Co_{75}Si_{15}B_{10}$; c) $Co_{75}Si_{15}B_{10}$; ASM – amorphous structure in metals, MCS – microcrystalline structure in metals, I – inoculants.

The formation of the ASM occurred due to a substantial increase in the heat extraction intensity. This high rate of cooling resulted in an amorphous-crystalline structure in the bulk interior, while pure ASM was successfully formed in the surface layers.

Fig. 7 presents the dependencies of the degree of amorphization Ψ on several key processing parameters: the mass ratio of inoculants to the melt (shown for both the minimum and maximum cooling water temperatures); the intensity of ultrasonic oscillations; the temperature of the inoculants.

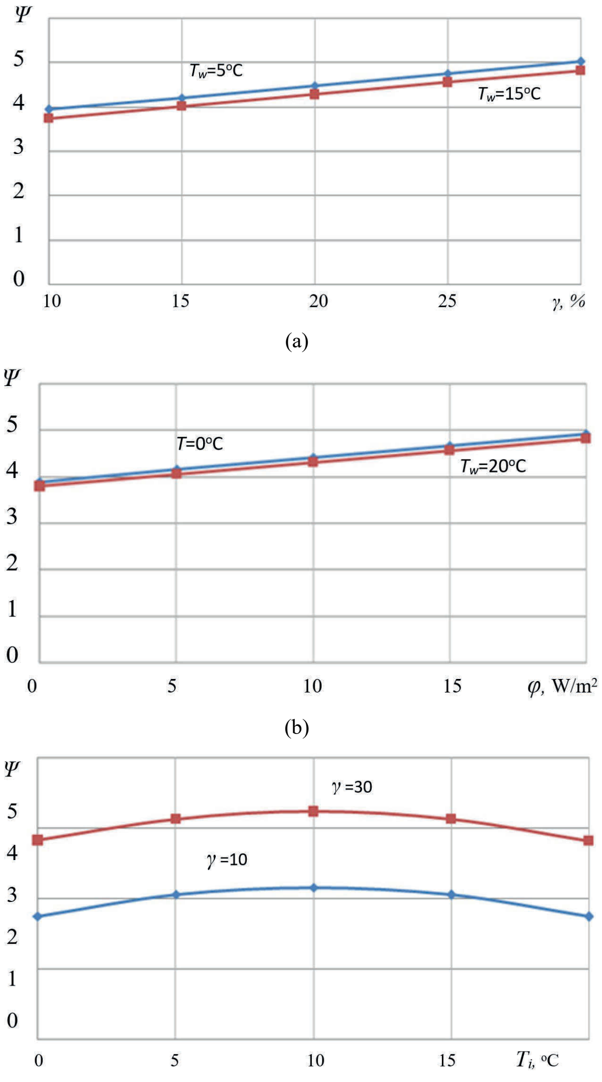

(a)

(b)

(c)

Fig. 7. Graphs of the degree of amorphization depending on: a) the ratio of the mass of the melt to the mass of the inoculators γ at different cooling water temperatures T_w; b) the intensity of ultrasonic vibrations φ at different inoculator temperatures; c) the inoculator temperature T_i.

4. DISCUSSION

The inoculants introduced into the melt extract heat through their own heating and subsequent melting, consequently reducing the overall melt temperature. As the mass ratio of inoculants to melt increases, the overall solidification rate is enhanced.

At a relatively low ratio of inoculant mass to the total melt mass (up to 10−15 %), the inoculants manage to almost completely dissolve due to the superheat within the liquid metal. Consequently, they exert no significant influence on the formation of the ASM during solidification. In this scenario, ASM formation is confined primarily to the vicinity of the boundary with the cooling medium.

In contrast, when the mass ratio of inoculants to the total melt mass is higher (20−30 %), the inoculants do not completely melt before the liquid phase begins to solidify. As a result, the latent heat of solidification is partially consumed by the heating and melting of these undissolved inoculants.

This mechanism reduces the quantity of heat released per unit volume of the melt with inoculants during solidification, leading to a further decrease in the melt temperature. The introduction of a larger quantity of inoculants is thus highly effective in lowering the melt temperature and promoting predominantly volumetric solidification.

The intensity of ultrasonic oscillations exhibits a positive influence on amorphous structure formation. During the solidification process, subjecting the metallic melt to ultrasonic treatment actively suppresses the formation of a crystalline structure near the mold's cooling walls and the interface with the cooling medium. This suppression prevents the crystallization front from fully propagating, which otherwise leads to a microcrystalline structure in the central region of the melt.

The application of ultrasonic vibration during casting solidification refines the microstructure and improves the mechanical properties of the metal. Furthermore, increasing the intensity of the ultrasonic oscillations induces agitation (mixing) within the melt and intensifies heat exchange processes. This action partially homogenizes the temperature distribution throughout the melt volume, which leads to a slight acceleration in the removal of superheat.

As observed from the graphs (Fig. 7), the influence of the initial inoculant temperature on the degree of amorphization Ψ is minor. Only a marginal decrease in the degree of amorphization is observed with increasing inoculant temperature.

Based on these experimental findings, it can be concluded that significantly pre-cooling the inoculants in this specific technology lacks practical significance and is not economically justified.

The cooling water temperature is a more significant factor influencing the degree of amorphization Ψ than the initial inoculant temperature. However, based on the experimental results, a substantial reduction in the cooling water temperature is deemed technologically and economically impractical. This conclusion is supported by the finding that only a marginal decrease in the degree of amorphization occurs when the water temperature is increased.

To achieve a bulk ASM using the current technology, the following operational parameters are considered optimal from both an economic and practical perspective:

- increasing the mass ratio of inoculants to the melt to approximately 20 %;
- reducing the intensity of ultrasonic oscillations to a medium level, utilizing the ultrasonic generator at maximum settings leads to excessive energy consumption, rendering it economically inefficient.
- maintaining moderate values for both the cooling water temperature and the initial inoculant temperature.

5. CONCLUSION

The application of inoculants in the technology for forming ASM effectively establishes internal heat sinks within the molten metal, ensuring accelerated heat extraction. This process allows for an increase in the overall cooling rate, which, as demonstrated, enables the formation of a thermodynamically unstable amorphous structure in certain alloys.

Of the alloys studied, the most interesting are massive amorphous alloys of the copper–titanium–zirconium system. With an increase in the Zr content to 18 %, the thermal stability of the alloy increases from 690 to 815 K, which significantly increases the scope of its application.

To create an amorphous structure and ensure the appropriate physical properties of the metal, various impurities can be introduced, for example, copper, aluminum or zirconium. Their presence reduces the cooling rate barrier at which an amorphous layer is formed from 10^6 to 103 K/s. In this case, the amorphization technology will be less energy-consuming, which is proven by experimental data on the basis of which a method for predicting the degree of amorphization of the structure was created.

The obtained experimental and calculation data showed that when using our method for the formation of an amorphous structure, a critical cooling rate of about 1000 K/s is sufficient for the indicated alloys. The use of this experimental casting method allows the formation of massive amorphous castings with a thickness of up to several millimeters.

Crucially, upon the moment of contact between the inoculant and the liquid metal, localized thermal undercooling is instantaneously generated in the melt. This localized effect occurs even when the overall melt volume retains significant superheat.

The proposed mathematical model successfully facilitates the analysis of the potential for ASM formation and allows for the determination and optimization of the critical operating parameters of the technological process.

REFERENCES

[1] Sharma A., Zadorozhnyy V. Y., Wenrui J., Qiao J. C. Review of hermo-mechanical processing of metallic glasses. *Journal of Non-Crystalline Solids* 2025:666:123714. https://doi.org/10.1016/j.jnoncrysol.2025.123714.

[2] Feng Z., Geng H., Zhuang Y., Li P. Progress, Applications, and Challenges of Amorphous Alloys: A Critical Review. *Inorganics* 2024:12(9):232. https://doi.org/10.3390/inorganics12090232

[3] Sohrabi S., Fu J., Li L., Zhang Y., Li X., Sun F., Ma J., Wang W. H. Manufacturing of metallic glass components: Processes, structures and properties. *Progress in Material Science* 2024:144:101283. https://doi.org/10.1016/j.pmatsci.2024.101283

[4] Cranford S. Mighty Morphin(g) Amorphous Metals. *Matter* 2020:2(4):802–804. https://doi.org/10.1016/j.matt.2020.03.008

[5] Zhang G., Hu H., Wu J. Advances in Amorphous Nanomaterials: Synthesis, haracterization and Application. *Materials Today Nano* 2025:32:100675. https://doi.org/10.1016/j.mtnano.2025.100675

[6] Kang J., Yang X., Hu Q., Cai Z., Liu L.-M., Guo L. Recent Progress of Amorphous Nanomaterials. *Chemical Reviews* 2023:123(13):8859–8941. https://doi.org/10.1021/acs.chemrev.3c00229

[7] Han X., Wu G., Du J., Pi J., Yan M., Hong X. Metal and metal oxide amorphous nanomaterials towards electrochemical applications. *Chemical Communications* 2022:58(2):223–237. https://doi.org/10.1039/D1CC04141J

[8] Gao K., Zhu X. G., Chen L., Li W. H., Xu X., Pan B. T., Li W. R., Zhou W. H., Li L., Huang W., Li Y. Recent development in the application of bulk metallic glasses. *Journal of Materials Science & Technology* 2022:131:115–121. https://doi.org/10.1016/j.jmst.2022.05.028

[9] Mahbooba Z., Thorsson L., Unosson M., Skoglund P., West H., Horn T., Rock C., Vogli E., Harrysson O. Additive manufacturing of an iron-based bulk metallic glass larger than the critical casting thickness. *Applied Materials Today* 2018:11:264–269. https://doi.org/10.1016/j.apmt.2018.02.011

[10] Zhu S., Schroers J., Curtarolo S, Eckert H, van de Walle A. Special glass structures for first principles studies of bulk metallic glasses. *Acta Materialia* 2024:262:119456. https://doi.org/10.1016/j.actamat.2023.119456

[11] Wu G., Han X., Hong X. Order in disordered monolayer carbon. *Matter* 2023:6(8):2528–2530. https://doi.org/10.1016/j.matt.2023.05.037

[12] Halim Q., Mohamed N. A., Rejab M. R., Naim W. N., Ma Q. Metallic glass properties, processing method and development perspective: a review. *The International Journal of Advanced Manufacturing Technology* 2021:112(5):1231–1258. https://doi.org/10.1007/s00170-020-06515-z

[13] Jiang R., Da Y., Chen Z., Cui X., Han X., Ke H., Liu Y., Chen Y., Deng Y., Hu W. Progress and perspective of metallic glasses for energy conversion and storage. *Advanced Energy Materials* 2022:12(8):2101092. https://doi.org/10.1002/aenm.202101092

[14] Assouli S., Jabraoui H., Bajjou O., Kotri A., Mazroui M. H., Lachtioui Y. Exploring the impact of cooling rates and pressure on fragility and structural transformations in iron monatomic metallic glasses: Insights from molecular dynamics simulations. *Journal of Non-Crystalline Solids* 2023:621:122623. https://doi.org/10.1016/j.jnoncrysol.2023.122623

[15] El hafi T., Bajjou O., Jabraoui H., Louafi J., Mazroui M. Lachtioui Y. Effects of cooling rate on the glass formation process and the microstructural evolution of Silver mono-component metallic glass. *Chemical physics* 2023:569:111873. https://doi.org/10.1016/j.chemphys.2023.111873.

[16] El kharraz A., El hafi T., Assouli S., Samiri A., Kotri A., Bajjou O., Lachtioui Y. Mechanical and structural properties of monatomic zirconium metallic glass under pressure variations and annealing processes: A molecular dynamics study. *Solid State Communications* 2024:392:115644. https://doi.org/10.1016/j.ssc.2024.115644

[17] Assouli S., El Hafi T., El Kharraz A., Bajjou O., Lachtioui Y. Influence of cooling rate and pressure on the structural and mechanical properties of iron monatomic metallic glasses: Insights from molecular dynamics simulations. *Solid State Communications* 2025:399:115883. https://doi.org/10.1016/j.ssc.2025.115883

[18] Pavlenko A., Koshlak H. Heat and mass transfer during phase transitions in liquid mixtures. *Rocznik Ochrona Srodowiska* 2019:21(1):234–249

[19] Koshlak H., Pavlenko A. Method of formation of thermophysical properties of porous materials. *Rocznik Ochrona Srodowiska* 2019:21(2): 1253–1262.

[20] Pavlenko A., Koshlak H. Intensification of Gas Hydrate Formation Processes by Renewal of Interfacial Area between Phases. *Energies* 2021:14(18):5912. https://doi.org/10.3390/en14185912

[21] Feng Z., Geng H., Zhuang Y., Li P. Progress, Applications, and Challenges of Amorphous Alloys: A Critical Review. *Inorganics* 2024:12(9):232. https://doi.org/10.3390/inorganics12090232

[22] Trexler M. M., Thadhani N. N. Mechanical properties of bulk metallic glasses. *Progress in Materials Science* 2010:55(8):759–839. https://doi.org/10.1016/j.pmatsci.2010.04.002

[23] Quan D., Jun T., Caiju L., Baran S., Jürgen E. Room-temperature plasticity of metallic glass composites: A review, Composites Part B. *Engineering* 2024:280:111453. https://doi.org/10.1016/j.compositesb.2024.111453

[24] Muscas G., Johansson R., George S., Martina A., Dimitri A., Rajeev A., Scheicher R. H., Jönsson P. E. Unveiling the local structure of the amorphous metal combining first-principles-based simulations and modelling of EXAFS spectra. *Scientific Reports* 2023:13:4983. https://doi.org/10.1038/s41598-023-32051-3

[25] Shen Y., Samwer K., Johnson W. L., Goddard W. A., An Q. Phase formation and phase stability for the homogenous and heterogeneous amorphous metals versus the crystalline phase. *Proc. Natl. Acad. Sci. U.S.A.* 2025:122(4):e2404489122. https://doi.org/10.1073/pnas.2404489122

[26] Cui C. Y., Liu X. F., Feng L., Xu H. H., Yang J., Cui X. G., Yan H. F. Effects of B content on the microstructure and corrosion resistance of laser cladding CoCrNiNb0.6Bx high-entropy alloy coatings. *Journal of Alloys and Compounds* 2025:1032:181085. https://doi.org/10.1016/j.jallcom.2025.181085

[27] Zhilin W., Xiao L., Siyi D., Lichen L., Liliang S., Yuqiang Y., Zhengwu P., Jing Z., Haibo K., Liejun L., Weihua W. A strong and plastic Fe-based composite alloy with extremely high saturation magnetic flux density by constructing multiscale heterogeneous structure. *Journal of Materials Science & Technology* 2026:240:156–165. https://doi.org/10.1016/j.jmst.2025.02.081

[28] Wang G., Zhang Y., Bingkun Z., Liu Y., Zheng S., Li X., Yan W., Li Z., Wang Y. M. Enhanced plasticity due to melt pool flow induced uniform dispersion of reinforcing particles in additively manufactured metallic composites. *International Journal of Plasticity* 2023:164:103591. https://doi.org/10.1016/j.ijplas.2023.103591

[29] Zhang L., Sun J., Ngan A. H. W., Ning Z., Fan H., Huang Y. Heterogeneity of microstructures in a Cu–Zr based amorphous alloy composite reinforced by crystalline phases, Composites Part B. *Engineering* 2023:262:110823. https://doi.org/10.1016/j.compositesb.2023.110823

[30] Pu Y., Liang Y., Zhou Y., Chen Q., Gao T., Zhou L., Tian Z. Micro-mechanism of mechanical enhancement of NiTiAl amorphous-crystal nanomultilayers. *International Journal of Mechanical Sciences* 2025:288:110020. https://doi.org/10.1016/j.ijmecsci.2025.110020

[31] Pavlenko A., Koshlak H. Production of porous material with projected thermophysical characteristics. *Metallurgical and Mining Industry* 2015:7(1):123–127.

[32] Pavlenko A., Koshlak H., Usenko B. The processes of heat and mass exchange in the vortex devices. *Metallurgical and Mining Industry* 2014:6(3):55–59.

[33] Pavlenko A., Koshlak H., Usenko B. Heat and mass transfer in fluidized layer. *Metallurgical and Mining Industry* 2014:6(6):96–100.

[34] Zhao W., Shan X., Kong X. R., Luo J., Li G. Quantitative analysis of the microstructure evolution of Al–Fe binary amorphous alloys caused by cooling rates based on atomic bond proportion. *Journal of Material Science* 2025:60:14160–14170. https://doi.org/10.1007/s10853-025-11236-3

[35] Zhao W., Cheng J. L., LI G. Quantitative analysis of structure evolution of Zr-Cu amorphous alloys caused by cooling rates based on atomic bond proportion. *Computational Materials Science* 2021:186:110011. https://doi.org/10.1016/j.commatsci.2020.110011

[36] He Y., Qin Y., Behmadi R., Hojati N., He Q., Chen C., Liu H., Yang W., Hojjati-Najafabadi A. Effect of cooling rate on the mechanical properties of amorphous alloy: From the perspective of heterogeneity. *Materials Letters* 2025:387:138239. https://doi.org/10.1016/j.matlet.2025.138239

[37] Radovanović-Perić F., Panžić I., Bafti A., Mandić V. Thermal and Thermomechanical Analysis of Amorphous Metals: A Compact Review. *Applied Sciences* 2024:14(17):7452. https://doi.org/10.3390/app14177452

[38] Li J., Lu W., Liu L., Fu L., Feng A. Study on crystal to amorphous transition of nickel-based alloy processed by ultra-short pulsed laser shock peening. *Materials Letters* 2024:366:136554. https://doi.org/10.1016/j.matlet.2024.136554.

[39] Lu W. N., Li J., Liu L., Ye Y. J., Pan H. J., Zhang Z., Feng A. X. Study on the spallation behavior of FeCoCrNiCu high-entropy alloy under laser shock peening at cryogenic temperature. *Materials Letters* 2025:388:138335. https://doi.org/10.1016/j.matlet.2025.138335

[40] Wang J., Xia J., Liu Z., Xu L., Liu J., Xiao Y., Gau J., Ru H., Jiao J. A comprehensive review of metal laser hardening: mechanism, process, and applications. *The International Journal of Advanced Manufacturing Technology* 2024:134:5087–5115. https://doi.org/10.1007/s00170-024-14463-1

[41] Senthil Kumar P., Jegadheesan C., Somasundaram P., Praveen Kumar S., Vivek Anand A., Singh A. P., Jeyaprakash N. Review on laser surface hardening of alloy metals. *Materials Today: Proceedings* 2023. https://doi.org/10.1016/j.matpr.2023.04.259

[42] Sahu A., Janardhan N., Amireddy K. K., Chinta V. S., Patnaik L., Singh L. K. Aluminum-Based Amorphous Alloys and Composites Synthesized Via Powder Metallurgy Route: A Review. *Powder Metallurgy and Metal Ceramics* 2025:63:654–669. https://doi.org/10.1007/s11106-025-00493-1

[43] Sun C., Zhou X., Lu J., Xie L., Li R., Wu Y., Dan X., Zhang M. Formation of Al-based Metallic Glasses Composites Prepared by Cold Spraying. *Journal of Thermal Spray Technology* 2022:31:1844–1859. https://doi.org/10.1007/s11666-022-01406-z

[44] Ratzker B., Sokol M. Exploring the capabilities of high-pressure spark plasma sintering (HPSPS): A review of materials processing and properties. *Materials & Design* 2023:233:112238. https://doi.org/10.1016/j.matdes.2023.112238

[45] Babalola B. J., Ayodele O. O., Olubambi P. A. Sintering of nanocrystalline materials: Sintering parameters. *Heliyon* 2023:9(3):e14070. https://doi.org/10.1016/j.heliyon.2023.e14070

[46] Pavlenko A., Usenko B., Koshlak A. Analysis of thermal peculiarities of alloying with special properties. *Metallurgical and Mining Industry* 2014:6(2):15–19.

[47] Lin T.-N., Liao P.-H., Wang C.-C., Lee H.-B., Tsay L.-W. Corrosion Resistance of Fe-Based Amorphous Films Prepared by the Radio Frequency Magnetron Sputter Method. *Materials* 2024:17(9):2071. https://doi.org/10.3390/ma17092071

[48] Liao P-H, Jian J-W, Tsay L-W. The Corrosion andWear-Corrosion of the Iron-Base Amorphous Coating Prepared by the HVOF Spraying. *Metals* 2023:13(6):1137. https://doi.org/10.3390/met13061137

[49] Nayak S. K., Faridi Md A., Gopi M., Kumar A., Laha T. Fe-based metallic glass composite coatings by HVOF spraying: Influence of Mo on phase evolution, wear and corrosion resistance. *Materials Characterization* 2022:191:112149. https://doi.org/10.1016/j.matchar.2022.112149

[50] Ning W., Zhai H., Xiao R., He D., Liang G., Wu Y., Li W., Li X. The Corrosion Resistance Mechanism of Fe-Based Amorphous Coatings Synthesised by Detonation Gun Spraying. *Journal of Materials Engineering and Performance* 2020:29:3921–3929. https://doi.org/10.1007/s11665-020-04876-w

[51] Basok B., Davydenko B., Pavlenko A. M. Numerical Network Modeling of Heat and Moisture Transfer through Capillary-Porous Building Materials. *Materials* 2021:14(8):1819. https://doi.org/10.3390/ma14081819

[52] Pavlenko A., Usenko B., Koshlak A. Thermal conductivity of the gas in small space. *Metallurgical and Mining Industry* 2014:6(2):20–24.

[53] Koshlak H., Pavlenko A. Mathematical model of particle free settling in a vortex apparatus. *Rocznik Ochrona Srodowiska* 2020:22(2):727–734.

[54] Radchenko M., Radchenko A., Trushliakov E., Pavlenko A., Radchenko R. Advanced Method of Variable Refrigerant Flow (VRF) Systems Designing to Forecast On-Site Operation – Part 1: General Approaches and Criteria. *Energies* 2023:16(3):1381. https://doi.org/10.3390/en16031381

[55] Pavlenko A. Peculiarities of Modelling of Vapour-Liquid Flows of Bubble Structure. *Environmental and Climate Technologies* 2025:29(1):128–136. https://doi.org/10.2478/rtuect-2025-0009

[56] Cao X., Zhang E., Bai X., Ji J., Sun J. Experimental Study on Temperature-time Characteristics of Loess under the Freeze-Thaw Cycles. *Environmental and Climate Technologies* 2025:29(1):84–96. https://doi.org/10.2478/rtuect-2025-0006